

Article

Properties on Yttrium-Doped/Undoped Barium Cerate and Barium Zirconate Thin Films Formed by E-Beam Vapor Deposition

Monica Susana Campos Covarrubias ^{1,*}, Mantas Sriubas ¹, Kristina Bockute ¹, Aurelija Poskaite ¹, Rokas Vazgys ¹, Maria Gazda ² and Giedrius Laukaitis ¹

¹ Physics Department, Kaunas University of Technology, Studentu Str. 50, LT-51368 Kaunas, Lithuania; mantas.sriubas@ktu.lt (M.S.); kristina.bockute@ktu.lt (K.B.); aurelija.poskaite@ktu.edu (A.P.); rokas.vazgys@ktu.edu (R.V.); giedrius.laukaitis@ktu.lt (G.L.)

² Institute of Nanotechnology and Materials Engineering, Faculty of Applied Physics and Mathematics, Advanced Materials Centre, Gdańsk University of Technology, Narutowicza 11/12, 80-233 Gdańsk, Poland; maria.gazda@pg.edu.pl

* Correspondence: monica.campos@ktu.lt

Abstract: As electrolyte materials for proton conductive fuel cells, perovskite-type materials such as barium cerates and barium zirconates have received a lot of attention due to their high protonic conduction at intermediate temperatures. Yet, the crystalline structure and the microstructure of the electrolyte layers are of the utmost importance that define the resulting protonic conductivity. The aim of this research was to investigate the formation of doped/undoped BCO and BZO thin films using e-beam vapor deposition and to analyze the influence of the formation parameters on the microstructural and crystallographic properties. Crystalline structure and microstructure were investigated by X-ray diffractometer and scanning electron microscope, while the elemental composition of the resulting thin films was analyzed by an energy-dispersive X-ray spectroscopy. It was found that the formed thin films were highly dense and consisted of the oriented columnar grains. The crystallinity of the thin films was strongly expressed with the predominant crystallographic orientations for undoped/doped barium cerates. Yttrium dopant had an influence on the lattice parameters and crystallite sizes. With the chosen technological parameters allowed to both, barium cerates and barium zirconates did not form carbonates and did not experience the degradation process.

Keywords: barium cerate; barium zirconate; e-beam evaporation; thin films; morphology; microstructure



Citation: Campos Covarrubias, M.S.; Sriubas, M.; Bockute, K.; Poskaite, A.; Vazgys, R.; Gazda, M.; Laukaitis, G. Properties on Yttrium-Doped/Undoped Barium Cerate and Barium Zirconate Thin Films Formed by E-Beam Vapor Deposition. *Appl. Sci.* **2022**, *12*, 6422. <https://doi.org/10.3390/app12136422>

Academic Editor:
Zakhar Kudrynskyi

Received: 17 May 2022

Accepted: 22 June 2022

Published: 24 June 2022

Publisher's Note: MDPI stays neutral with regard to jurisdictional claims in published maps and institutional affiliations.



Copyright: © 2022 by the authors. Licensee MDPI, Basel, Switzerland. This article is an open access article distributed under the terms and conditions of the Creative Commons Attribution (CC BY) license (<https://creativecommons.org/licenses/by/4.0/>).

1. Introduction

Thin films as the membranes for the potential application in fuel cells are increasingly gaining scientific attention due to their capacities to decrease the operating temperature to the intermediate temperatures, reduce the internal resistance, and as a consequence, increase the conductivity [1]. The main proton-conducting oxides currently being studied as proton-conducting electrolytes are barium cerates BaCeO₃ (BCO), and barium zirconates BaZrO₃ (BZO) or strontium cerates (SrCeO₃).

Alkaline cerates (ACeO₃) and zirconates (AZrO₃) are the main materials for the protonic conductivity of perovskite oxides (A, in this case, is an alkaline earth metal (Ca, Sr or Ba)). In barium or strontium cerates, rare earth elements such as Yb, Gd, Nd, and Y are the most common dopants due to their ionic radii size closeness to cerium or zirconium [2]. In various studies [3–5], these cerates have shown a relatively high protonic conductivity, but also react in acidic environments to form carbonates in environments with CO₂ and H₂O. Zirconates are more chemically stable and have better mechanical properties, react poorly in acidic environments, are stable in a CO₂ environment, but have a significantly lower proton conductivity [6,7]. Different approaches were made to find the best combination

of a high protonic conductivity and a high chemical and mechanical stability, such as the modifications of technological parameters or the incorporation of the different dopant concentrations [4,8,9]. Proton conductivity values and other physical properties in barium cerates and zirconates depend significantly not only on the type or concentration of dopants, but also on the methods of thin film formation that can determine the resulting structural composition, microstructure, and other physical properties influencing the proton diffusion and conductivity, such as density and grain size [4,10,11]. Knowing that the electrolytes may have a different microstructure, density, and crystallinity depending on the chosen formation method, it is important to analyze the formation methods and technological parameters to obtain highly dense and crystalline films with the predictable microstructure. In addition, it is important to understand the influence of dopants and their different concentrations that may also affect the chemical stability, phase, lattice parameters, grain size, and strains of the materials [4]. Moreover, a low crystallinity adds resistance to the ion conductivity [7]. Therefore, highly dense electrolytes with a high crystallinity are required. The proton jump energy is also influenced by lattice parameters that differ for BCO and BZO, e.g., $a = 8.724 \text{ \AA}$, $b = 6.230 \text{ \AA}$, and $c = 6.211 \text{ \AA}$ of BCO [8] and $a = 4.210 \text{ \AA}$ [9] of BZO.

The main aim of this research is to investigate the formation of doped/undoped BCO and BZO thin films using e-beam vapor deposition and to analyze the influence of the formation parameters on the microstructural and crystallographic properties.

2. Materials and Methods

Barium zirconate and barium cerate thin films were deposited using e-beam physical vapor deposition system “Kurt J. Lesker EB-PVD 75”, (Kurt J. Lesker Company GmbH, Frankfurt, Germany). The initial powders, (Goodfellow Cambridge Ltd, Huntingdon, UK) (BCO, 99.9% purity; barium cerate doped with 10% (BCY10) and 20% yttrium (BCY20), 99.9% purity, BZO, 99.9% purity; barium zirconate doped with 20% yttrium (BZY20), and barium zirconate doped with yttrium and cerium (BZCY), 99.9% purity) were used as target materials to form the thin films. The powders were pressed into pellets and evaporated on substrates made of Inconel alloy 600 (Ni72/Cr16/Fe8), (Goodfellow Cambridge Ltd, Huntingdon, UK). Prior to the deposition, substrates were cleaned ultrasonically with isopropanol and acetone. During the deposition, the temperature of substrate was kept constant at 500 °C. The acceleration voltage of the electron gun was 7.9 kV, the current was adjusted in the range of 30–100 mA with a deposition rate of 2 Å/s. The initial pressure was 1×10^{-5} Pa and the working pressure range was from 1×10^{-3} Pa to 1×10^{-4} Pa.

The resulting thin films had a thickness of ~2.0 µm for all deposited samples. The thickness was measured with a profilometer Ambios Technology XP-200, (Ambios Technology Inc., Santa Cruz, CA, US). Density of the thin film was calculated using the mass of the thin film and its thickness. The crystalline structure of the thin films was studied by an X-ray diffractometer (XRD) “Bruker D8 Discover”, (Bruker AXS GmbH, Billerica, MA, USA). The phase identification was performed using PDF-2 database. Crystal size and lattice parameters were obtained by refinement of the acquired diffraction pattern via the Le Bail method, using TOPAS 4.2 software (Bruker, Karlsruhe, Germany). The measurements were performed using Cu Kα ($\lambda = 0.154059 \text{ nm}$) radiation at a geometry of 2Θ angle in a 20° – 70° range and a 0.01° step. The texture coefficients that describe the preferential crystallite orientation in the thin films were calculated using the following equation:

$$TC_{(h_i, k_i, l_i)} = \frac{I(h_i, k_i, l_i)}{I_0(h_i, k_i, l_i)} \left\{ \frac{1}{N} \sum_{i=1}^N \frac{I(h_i, k_i, l_i)}{I_0(h_i, k_i, l_i)} \right\}^{-1} \quad (1)$$

where $I(h_i, k_i, l_i)$ is the intensity of (h_i, k_i, l_i) peak.

The surface topography and cross-section images were obtained using the scanning electron microscope (SEM) “Hitachi S-3400N”, (Hitachi High-Technologies, Tokyo, Japan). The elemental composition was estimated using an energy-dispersive X-ray spectroscope (EDS) “BrukerXFlash QUAD 5040”, (Bruker AXS GmbH, Billerica, MA, USA). Grain size

distribution was evaluated by ImageJ software 1.53K (Wayne Rasband and contributors, National Institute of Health, MA, USA).

3. Results and Discussion

The e-beam evaporation of thin films is an atomistic process, where atoms and molecules involved in the deposition in the vapor state chemically or physically adsorb on the surface of the substrate and eventually form a thin film following the thin film evaluation steps of nucleation, crystal/grain growth, coalescence, grain coarsening, and phase transformations [12]. The morphology of the resulting thin films largely depends on the substrate temperature, the deposition parameters, and the composition of the evaporated material. At an evaporation of metal oxides, the elemental composition of the thin films may differ from the initial material in the crucible. A variation in composition changes the thermochemical properties of each material and affects the diffusion towards microstructure formation [13]. In case of the deposition of complex compounds, the deviation in elemental composition of the formed thin films and initial material may occur due to the different evaporation rates of the chemical elements in the compound (Table 1). Such deviations can be minimized to the level of obtaining very close stoichiometry of the thin films compared to the initial material by adjusting the deposition parameters, such as the e-beam current, the substrate temperature, etc. Here, the microstructural and crystallographic properties are investigated by keeping technological parameters constant and depositing different compounds; therefore, a relatively larger difference in the elemental composition is observed for the doped compounds.

Table 1. Elemental composition of the formed thin films and initial material.

	Ba, at.%	Zr, at.%	Ce, at.%	Y, at.%	O, at.%	Relative Density, %
BCO thin films	9.6	-	9.2	-	81.3	92
BCO initial powder	18.7	-	9.0	-	72.3	
BCY10 thin films	10.3	-	7.5	1.1	81.1	86
BCY10 initial powder	20.0	-	8.8	2.0	69.2	
BCY20 thin films	10.1	-	6.0	1.5	82.4	90
BCY20 initial powder	15.6	-	9.6	3.0	71.8	
BZO thin films	14.0	10.2	-	-	75.9	95
BZO initial powder	15.4	13.8	-	-	70.8	
BZCY thin films	13.3	12.8	1.0	2.8	70.2	87
BZCY initial powder	13.9	8.9	2.8	1.1	73.4	
BZY20 thin films	13.7	8.1	-	1.1	77.0	90
BZY20 initial powder	13.7	10.8	-	2.5	73.0	

The formed thin films were dense, and the density ranged from 86 to 92% of the relative density for undoped/doped barium cerate thin films and from 87 to 95% of the relative density for undoped/doped barium zirconate thin films compared to their theoretical densities [14–17]. The high density is attributed to the formation of the vapor phase in its neutral form that is deposited in the substrate. A low deposition rate minimizes the collisions between the evaporated particles to generate a less dense vapor cloud above the crucible. However, accelerated electrons from the e-beam gun can interact with the high dense cloud to generate partial ionization and create defects on the film [18]. The vapor cloud density also is influenced by the evaporated material [19].

The growth of the thin films and the resulting microstructure can be described by several structure zone models (SZM), such as Movchan and Demichishin [20], Thornton [21], and modified SZMs for specific compounds or formation methods [22,23]. The SZMs may give a qualitative guideline to the thin film growth processes during the deposition that can be altered by changes in the technological parameters. The formed thin films consisted

of oriented columnar grains defined by the grain boundaries. The microstructure of the formed thin was influenced by the dopants in the grain size and shape of the thin films. Thin films of BCO, BCY10, and BCY20 consisted of randomly oriented large grains with the shape of a triangular prism, growing on top of each other in the columnar way (Figure 1a–c) while BZO's and BZY's microstructures are contained in small circular-shaped grains (Figure 1d,e). Figure 1f demonstrates that even a small amount of cerium dopant influences the formation of the randomly oriented triangular grains instead of the circular-shaped grains. Such a polycrystalline orientation is expected for perovskite materials barium cerates and barium zirconates [24]. The grain size distribution performed by image processing software revealed that the addition of yttrium decreased the surface grain size of barium cerates, from 0.33 to 0.20 μm , on average. The surface grain sizes of barium zirconates were smaller than barium cerates, yet the same tendency of the grain size decrease in the thin films doped with yttrium was observed, from 0.14 to 0.07 μm , on average. Similar tendencies are seen in the research of M. Amsif et al. [25]. Cross sectional images (Figure 2) confirm the densely packed microstructure of barium cerates and zirconates independently of their composition. According to the Thornton structural model, the columnar growth of dense barium cerate thin films with expressed grain boundaries is observed and the films may be considered at zone II, which is characteristic when the ratio of the substrate temperature (T_s) and the material's melting temperature (T_m) is higher than 0.4 (Figure 2a–c). In such a condition, surface and bulk diffusion becomes substantial, resulting in the formation of large, oriented grains [20]. On the other hand, barium zirconate thin films were formed in zone T, which is denser than zone II (Figure 2d–f).

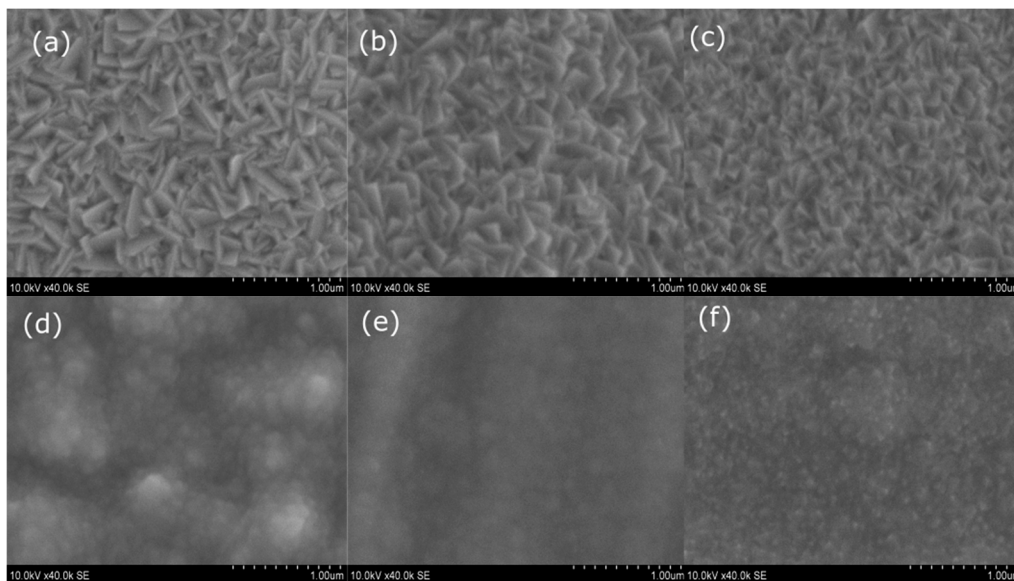


Figure 1. SEM images of the surface of the thin films: BCO (a), BCY10 (b), BCY20 (c), BZO (d), BZY20 (e), and BZCY (f).

An effect of the dopant on the roughness of barium zirconates can be seen from SEM images (Figure 2). The roughness was reduced with the addition of yttrium or cerium. Roughness can be created by charged particles of high energy that reach the surface that results in etching effects in some areas. The roughness can be reduced by enhancing the mobility of the depositing atoms or by low-energy ion bombardment during the deposition [26].

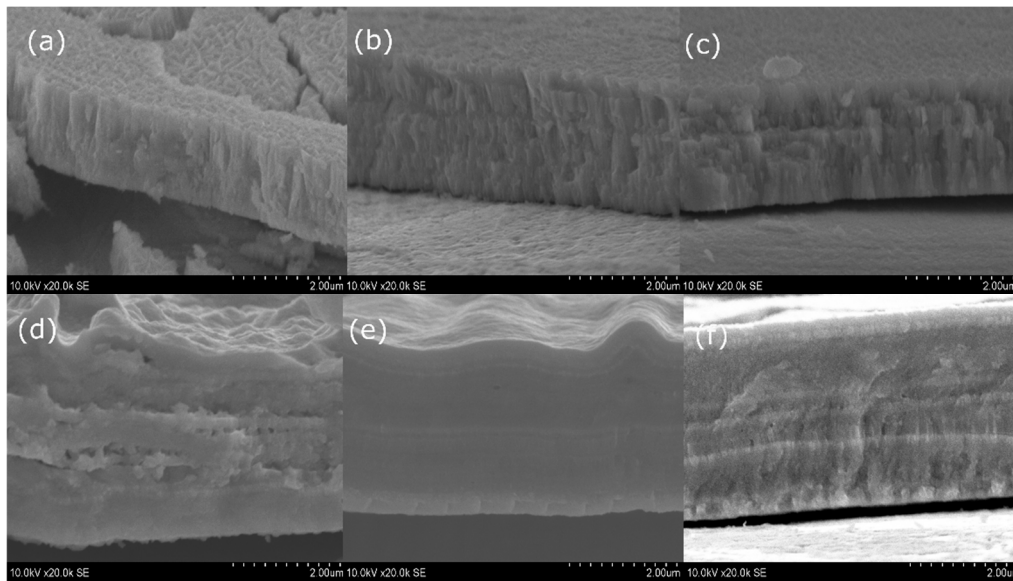


Figure 2. SEM cross-sectional images of the thin films: BCO (a), BCY10 (b), BCY20 (c), BZO (d), BZY20 (e), and BZCY (f).

It is known that one of the disadvantages of barium cerates and zirconates is their high reactivity with their environment and further degradation to the carbonates. The main sources of degradation are: (1) unreacted BaO that reacts with CO₂ and causes disintegration of the film [27], (2) amorphous phases that contain not very well packed regions and are usually found on the grain boundaries [28,29] that add free space to carbon molecules to enter, and (3) the high basicity of BaCeO₃ that makes it prone to react with CO₂ [30] above 400 °C. In order to verify the stability of the formed thin films, the crystallographic nature of the deposited films was measured twice: as deposited and after two weeks. The samples did not show any signs of degradation at room temperature. XRD identified that the BCO thin films deposited at a substrate's temperature of 500 °C had a predominant orthorhombic phase (PDF: 01-078-4102) with (002), (213) (231), and (004) (422) orientations (Figure 3a). The films were highly oriented towards the (002) plane. A crystallite size of 106.2 nm was calculated from Rietveld refinement and the Le Bail method (Table 2). This value was higher compared to the BCO pellets after sintering at high temperatures [31,32], with values between 30 and 75 nm. The high orientation is attributed to the orientation of the metal substrate alloys and e-beam formation conditions [33] (e.g., power and temperature). BCO-based oriented films formed by physical vapor deposition are usually reported as pseudocubic [34] or cubic [35]. Our results showed that with an increase in the crystallinity of an orthorhombic phase, a highly oriented film was formed compared with semi crystalline films with the "pseudocubic phase" reported before. Differences in FWHM values for the film and powder were 0.17264 and 0.18829, respectively, demonstrating the enhancement of the crystallinity for the film. The XRD pattern of as deposited BCY10 with an orthorhombic [23] *Pn*cm (PDF 01-083-5709) structure (Figure 3b) demonstrates a highly oriented crystallographic structure towards (002) and (213) (231). The high orientation is attributed to the orientation of the metal substrate [28], the e-beam formation conditions [36] that influence the crystallographic direction of the lowest surface energy and atomic composition [37], and it is associated with the increased number of grains along that plane, density and crystallinity [38], thickness, strain that can induce rotation, and the templated growth process [39]. Similar XRD patterns for BCY10 were observed in the thin film prepared by PLD at 750 °C [40]. Figure 3b also shows the XRD pattern of the BCY20 *Pm*-3*m* phase (PDF 01-084-7856). An orthorhombic *Im*ma [41] phase was reported when the samples were sintering in vacuum. Others report the formation of a rhombohedral phase [13] with a secondary Y_{0.2}Ce_{0.8}O_{1.9} phase. An increase in the yttrium amount results

in lower crystallite sizes being 24.2 nm and 10.3 nm for BCY10 and BCY20, respectively. FWHM values for BCO were lower (<0.4) compared to BCY10 and BCY20 (>0.5). The orientation direction changes with the percentage of concentration of the dopant due to a change in phase from orthorhombic to cubic. At a 10% yttrium concentration the predominant orientations are (024) (132), while only the (211) orientation remains predominant for the thin films with a 20% yttrium concentration. The preferential crystallographic orientations of the formed thin films are presented by the texture coefficients (Table 2).

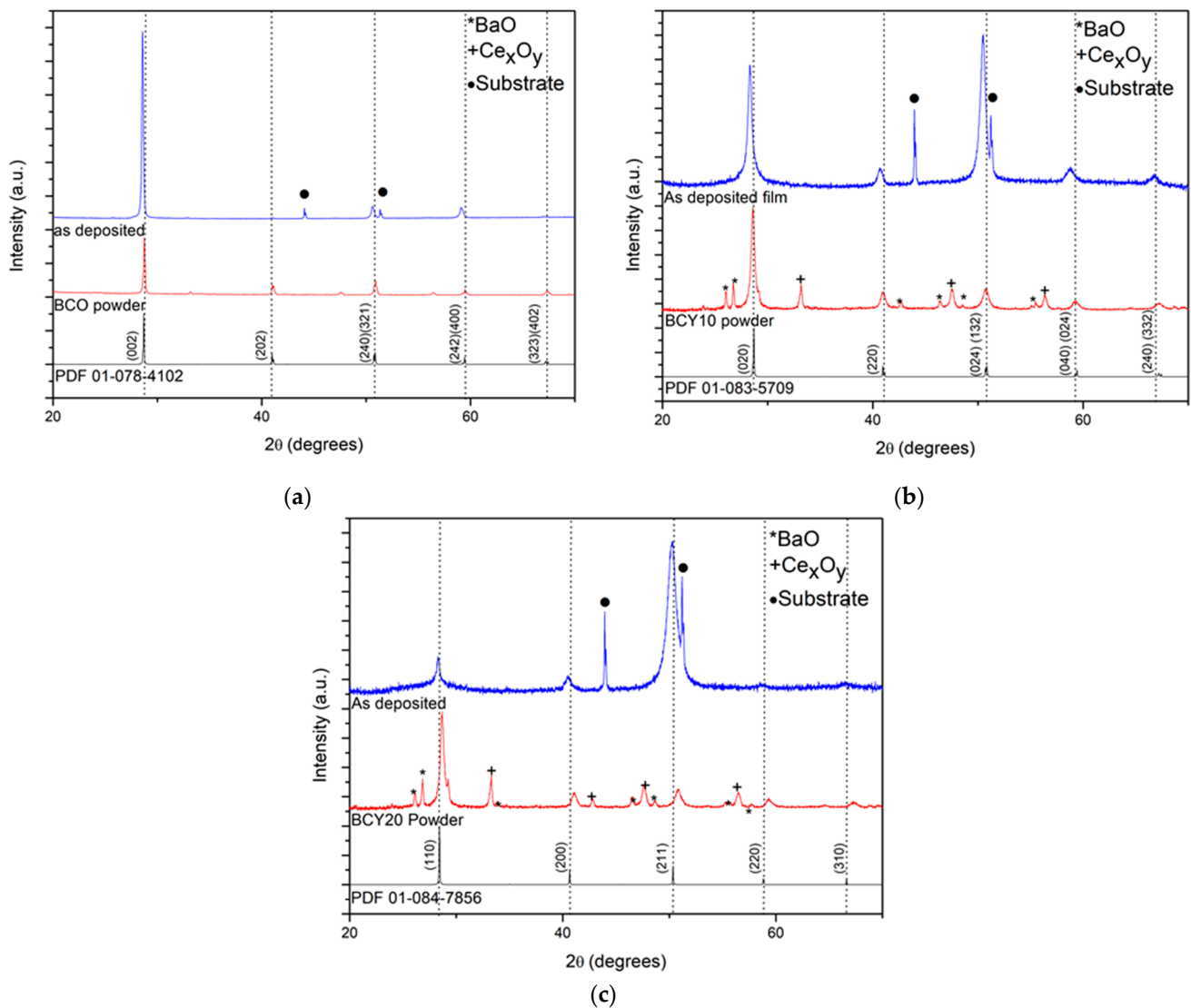


Figure 3. XRD patterns of (a) BCO thin films and initial powder; (b) BCY10 thin films and initial powders; and (c) BCY20 thin films and initial powder.

Table 2. Texture coefficients of the formed thin films.

Thin Films	Referential PDF Card	Crystallographic Phase	Texture Coefficients for the Expressed Crystallographic Orientations				
			(002)	(202)	(240) (321)	(242) (400)	(323) (402)
BCO	01-078-4102	<i>Pnma</i>	2.89	0.05	0.73	1.20	0.11
BCY10	01-083-5709	<i>Pbnm</i>	0.55	0.38	3.06	0.48	0.50
BCY20	01-084-7856	<i>Pm-3m</i>	0.89	0.15	1.95		

However, the BZO thin films do not show a single barium zirconate structure, but consist of barium carbonate, BaO, and Ba₃Zr₂O₇, which partially overlaps with BaZrO₃ (Figure 4). Similarly, the BZY20 and BZCY thin films exhibit structures with additional oxides and carbonates. Such a mixture of phases can arise due to several reasons, one of them being the non-stoichiometry of the formed thin films and atomistic deposition by e-beam evaporation, in addition to the too low deposition temperature and a lack of further annealing. It is known that BaO reacts easily with the atmosphere towards the formation of BaCO₃ [27]. Therefore, a higher energy is needed to break the bond on the oxides. Additionally, oxygen vacancies enhance the diffusion [42]. At the end, a mixture of these two effects is involved in the diffusion process. These results suggest that an increase in temperature and power should be necessary to enhance the diffusion to obtain barium zirconates without additional phases. The crystallite size values were 12.0 nm and 8.6 nm for BZO and BZY20, respectively.

It is known that a high power in an e-beam vapor deposition enhances the crystallinity and crystal size of the structures [43,44]. Another parameter that results in the enhanced crystallinity is the thickness of the formed thin films. A thin film growth and crystallization occur by the formation of nucleation centers and their growth that are dependent on the thickness of the thin film. Crystal growth is then controlled by volume diffusion and the free energy change of a system that acts as its driving force [45]. Moreover, the microstructure of the formed thin films suggests that a repeated surface nucleation may happen due to chosen technological parameters. The deposition temperature also contributes to the enhancement in crystal growth [35]. In addition, the chosen formation method leads to different properties of the formed thin films, for example, pulsed laser deposition results in nanocolumnar growth and high crystalline nanostructures' formation due to the high energetic plasma that reaches the substrates [46–52], whereas the ionization region in the e-beam does not reach the substrate [52]. When the constant deposition parameters are kept, the crystallite size depends on the compound, lattice strains, structural imperfections, additional phases, etc. The lattice parameters and crystallite sizes were calculated for each material and summarized in Table 3. It is seen that the yttrium dopant influences the lattice parameters and crystallite sizes. Crystallite size values for barium cerate decreased with the content of yttrium from 106.2 nm to 10.3 nm. A similar trend was observed in barium zirconates; the crystallite size values for barium zirconate decreased with yttrium content from 12.0 nm to 8.6 nm. The lattice parameter increases with the addition of yttrium dopant for cubic phase with values of 4.2436 and 4.2446 nm for BZO and BZY20, respectively. Those values are slightly higher than the reported [53–55].

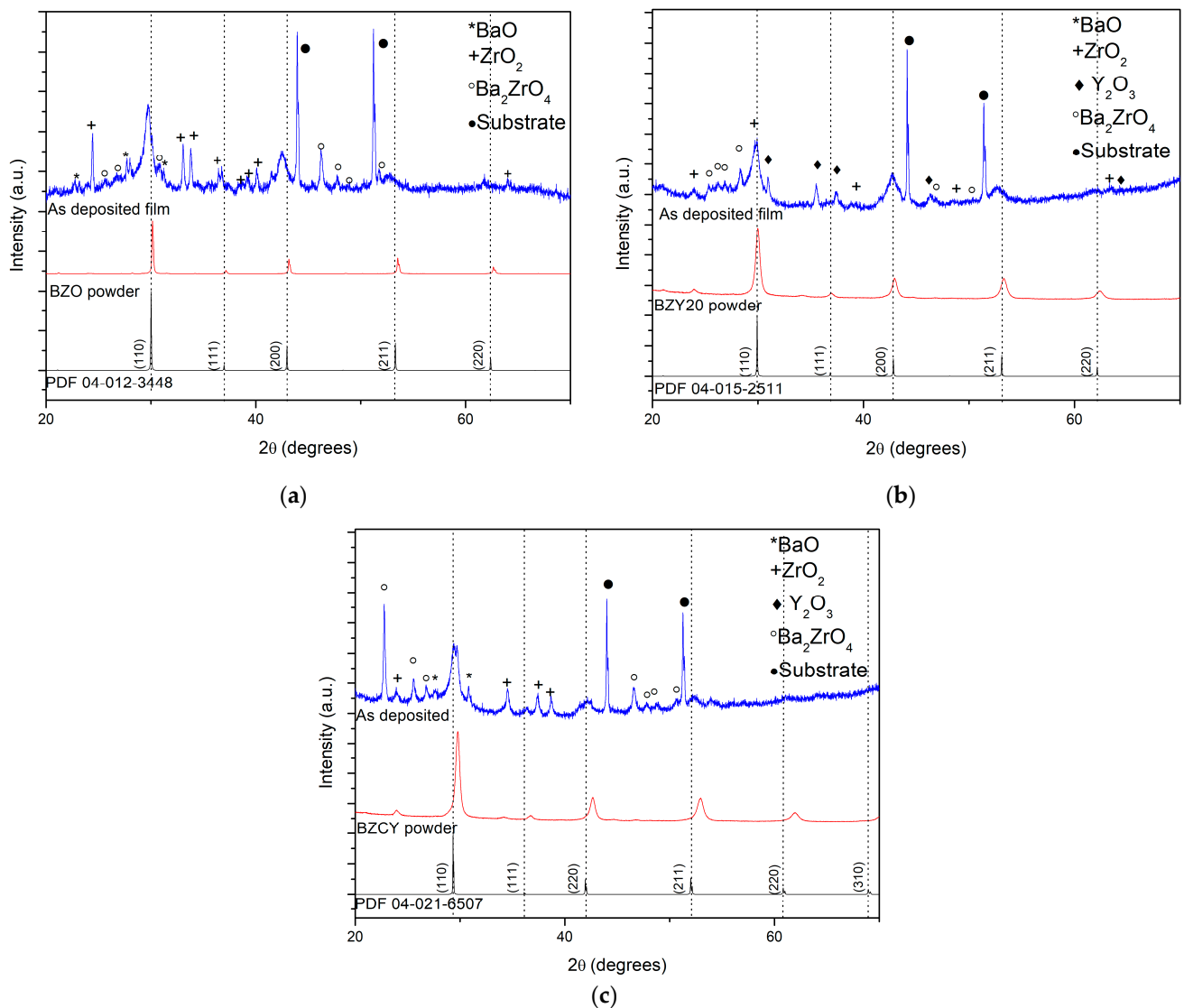


Figure 4. XRD patterns of (a) BZO thin films and initial powder; (b) BZY20 thin films and initial powders; and (c) BZCY thin films and initial powder.

Table 3. Lattice parameters and crystallite sizes of the formed thin films in comparison to the initial powder material's lattice parameters and crystallite sizes.

	Formed Thin Film				Powder			
	Crystallite Size, nm	Lattice Parameter, Å			Crystallite Size, nm	Lattice Parameter, Å		
		<i>a</i>	<i>b</i>	<i>c</i>		<i>a</i>	<i>b</i>	<i>c</i>
BCO	106.2	8.8116	6.2793	6.2580	122.0	8.7742	6.2339	6.2127
BCY10	24.2	8.6764	6.2473	6.3033	29.5	8.7031	6.1464	6.2138
BCY20	10.3	4.4393			16.8	4.4027		
BZO	12.0	4.2436			125.0	4.1915		
BZY20	8.6	4.2446			23.9	4.2169		
BZCY	2.4	4.3022			24.1	4.2437		

4. Conclusions

Highly dense microstructures of barium cerates and barium zirconates were successfully formed by e-beam vapor deposition at low deposition rates and 500 °C. The formed thin films consisted of oriented columnar grains. It was determined that the yttrium dopant reduces the grain size of the formed thin films. XRD measurements revealed that the

formed barium cerate films had a predominant orthorhombic phase. In addition, yttrium dopant had an influence on the lattice parameters, the crystallite sizes, and the preferential crystallographic orientation. The crystallite size values for barium cerate decreased with the content of yttrium from 106.2 nm for undoped BCO to 10.3 nm for BCY20. Contrary, the crystallite size values for barium zirconate increased with the yttrium content from 2.4 nm for BZCY to 8.6 nm for BZY20. Barium zirconates formed at 500 °C were composed of a mixture of phases, consisting of the oxides and carbonates. A higher power, a higher temperature during the deposition, or a smaller thickness are necessary to enhance the diffusion and crystal growth for these materials.

Author Contributions: Conceptualization, M.G. and G.L.; formal analysis, M.S.C.C., M.S., K.B., A.P. and R.V.; investigation, M.S.C.C. and M.S.; writing—original draft preparation, M.S.C.C., A.P. and R.V.; writing—review and editing, K.B. and G.L.; supervision, M.G. and G.L.; funding acquisition, M.G. and G.L. All authors have read and agreed to the published version of the manuscript.

Funding: The research was financially supported by Research Council of Lithuania (LMTLT), agreement No. S-LL-18-3 and the National Science Centre, Poland project No. 2017/27/L/ST5/03185.

Institutional Review Board Statement: Not applicable.

Informed Consent Statement: Not applicable.

Data Availability Statement: Not applicable.

Conflicts of Interest: The authors declare no conflict of interest.

References

1. Seo, H.G.; Choi, Y.; Koo, B.; Jang, A.; Jung, W. Robust nano-architected composite thin films for a low-temperature solid oxide fuel cell cathode. *J. Mater. Chem. A* **2016**, *4*, 9394–9402. [\[CrossRef\]](#)
2. Traversa, E.; Fabbri, E. Proton Conductors for Solid Oxide Fuel Cells (SOFCs). In *Functional Materials for Sustainable Energy Applications*; Woodhead Publishing Series in Energy; Kilner, J.A., Skinner, S.J., Irvine, S.J.C., Edwards, P.P., Eds.; Woodhead Publishing: Sawston, UK, 2012; pp. 515–537.
3. Rashid, N.L.R.M.; Samat, A.A.; Jais, A.A.; Somalu, M.R.; Muchtar, A.; Baharuddin, N.A.; Isahak, W.N.R.W. Review on zirconate-cerate-based electrolytes for proton-conducting solid oxide fuel cell. *Ceram. Int.* **2019**, *45*, 6605–6615. [\[CrossRef\]](#)
4. Rasaki, S.A.; Liu, C.; Lao, C.; Chen, Z. A review of current performance of rare earth metal-doped barium zirconate perovskite: The promising electrode and electrolyte material for the protonic ceramic fuel cells. *Prog. Solid State Chem.* **2021**, *63*, 100325. [\[CrossRef\]](#)
5. Hossain, M.K.; Chanda, R.; El-Denglawey, A.; Emrose, T.; Rahman, M.T.; Biswas, M.C.; Hashizume, K. Recent progress in barium zirconate proton conductors for electrochemical hydrogen device applications: A review. *Ceram. Int.* **2021**, *47*, 23725–23748. [\[CrossRef\]](#)
6. Bae, K.; Lee, S.; Jang, D.Y.; Kim, H.J.; Lee, H.; Shin, D.; Son, J.-W.; Shim, J.H. High-Performance Protonic Ceramic Fuel Cells with Thin-Film Yttrium-Doped Barium Cerate–Zirconate Electrolytes on Compositionally Gradient Anodes. *ACS Appl. Mater. Interfaces* **2016**, *8*, 9097–9103. [\[CrossRef\]](#) [\[PubMed\]](#)
7. Di Bartolomeo, E.; D’Epifanio, A.; Yang, N.; Tebano, A.; Balestrino, G.; Licocchia, S. Yttrium Doped Barium Cerate and Zirconate Heterostructures: Deposition and Electrochemical Characterization. *ECS Trans.* **2013**, *57*, 1059–1068. [\[CrossRef\]](#)
8. Fabbri, E.; D’Epifanio, A.; Di Bartolomeo, E.; Licocchia, S.; Traversa, E. Tailoring the Chemical Stability of $\text{Ba}(\text{Ce}_{0.8-x}\text{Zr}_x)\text{Y}_{0.2}\text{O}_{3-\delta}$ Protonic Conductors for Intermediate Temperature Solid Oxide Fuel Cells (IT-SOFCs). *Solid State Ion.* **2008**, *179*, 558–564. [\[CrossRef\]](#)
9. Katahira, K.; Kohchi, Y.; Shimura, T.; Iwahara, H. Protonic conduction in Zr-substituted BaCeO_3 . *Solid State Ion.* **2000**, *138*, 91–98. [\[CrossRef\]](#)
10. Beckel, D.; Bieberle-Hütter, A.; Harvey, A.; Infortuna, A.; Muecke, U.P.; Prestat, M.; Rupp, J.L.M.; Gauckler, L.J. Thin films for micro solid oxide fuel cells. *J. Power Sources* **2007**, *173*, 325–345. [\[CrossRef\]](#)
11. Lyu, Y.; Wang, F.; Wang, D.; Jin, Z. Alternative preparation methods of thin films for solid oxide fuel cells: Review. *Mater. Technol.* **2020**, *35*, 212–227. [\[CrossRef\]](#)
12. Barna, P.B.; Adamik, M. Growth Mechanisms of Polycrystalline Thin Films. In *Science and Technology of Thin Films*; World Scientific: Singapore, China, 1995; pp. 1–28.
13. Anders, A. (Ed.) Film Deposition by Energetic Condensation. In *Cathodic Arcs: From Fractal Spots to Energetic Condensation*; Springer: New York, NY, USA, 2008; pp. 363–407.
14. Subramaniyan, A.; Tong, J.; O’Hayre, R.P.; Sammes, N.M. Sintering Studies on 20 mol% Yttrium-Doped Barium Cerate. *J. Am. Ceram. Soc.* **2011**, *94*, 1800–1804. [\[CrossRef\]](#)
15. Boschini, F.; Robertz, B.; Rulmont, A.; Cloots, R. Preparation of nanosized barium zirconate powder by thermal decomposition of urea in an aqueous solution containing barium and zirconium, and by calcination of the precipitate. *J. Eur. Ceram. Soc.* **2003**, *23*, 3035–3042. [\[CrossRef\]](#)

16. Tong, J.; Clark, D.; Bernau, L.; Subramanian, A.; O'Hayre, R. Proton-conducting yttrium-doped barium cerate ceramics synthesized by a cost-effective solid-state reactive sintering method. *Solid State Ion.* **2010**, *181*, 1486–1498. [[CrossRef](#)]
17. Ricote, S.; Bonanos, N.; de Lucas, M.M.; Caboche, G. Structural and conductivity study of the proton conductor $\text{BaCe}_{(0.9-x)}\text{Zr}_x\text{Y}_{0.1}\text{O}_{(3-\delta)}$ at intermediate temperatures. *J. Power Sources* **2009**, *193*, 189–193. [[CrossRef](#)]
18. Bhatia, M.S.; Patel, K.; Joshi, A.; Chatterjee, U.K. Control of Ionization in E-beam Evaporators via Optimum Choice of Focus-coil Current. *Rev. Sci. Instrum.* **1989**, *60*, 2794–2796. [[CrossRef](#)]
19. Mukherjee, J.; Dileep Kumar, V.; Yadav, S.P.; Barnwal, T.A.; Dikshit, B. Plasma Diagnosis as a Tool for the Determination of the Parameters of Electron Beam Evaporation and Sources of Ionization. *Meas. Sci. Technol.* **2016**, *27*, 075007. [[CrossRef](#)]
20. Thornton, J.A. High Rate Thick Film Growth. *Annu. Rev. Mater. Sci.* **1977**, *7*, 239–260. [[CrossRef](#)]
21. Messier, R.; Giri, A.P.; Roy, R.A. Revised structure zone model for thin film physical structure. *J. Vac. Sci. Technol. A* **1984**, *2*, 500–503. [[CrossRef](#)]
22. Mirica, E.; Kowach, G.; Du, H. Modified Structure Zone Model to Describe the Morphological Evolution of ZnO Thin Films Deposited by Reactive Sputtering. *Cryst. Growth Des.* **2004**, *4*, 157–159. [[CrossRef](#)]
23. Thornton, J.A. Structure-zone models of thin films. In *Modeling of Optical Thin Films*; SPIE: San Diego, CA, USA, 1988; Volume 0821.
24. Jia, C.L.; Urban, K.; Mertin, M.; Hoffmann, S.; Waser, R. The Structure and Formation of Nanotwins in BaTiO_3 Thin Films. *Philos. Mag. A* **1998**, *77*, 923–939. [[CrossRef](#)]
25. Amsif, M.; Marrero-Lopez, D.; Ruiz-Morales, J.C.; Savvin, S.N.; Gabás, M.; Nunez, P. Influence of rare-earth doping on the microstructure and conductivity of $\text{BaCe}_{0.9}\text{Ln}_{0.1}\text{O}_{3-\delta}$ proton conductors. *J. Power Sources* **2011**, *196*, 3461–3469. [[CrossRef](#)]
26. Panjan, P.; Drnovšek, A.; Mahne, N.; Čekada, M.; Panjan, M. Surface Topography of PVD Hard Coatings. *Coatings* **2021**, *11*, 1387. [[CrossRef](#)]
27. Yamazaki, Y.; Hernandez-Sanchez, R.; Haile, S.M. Cation non-stoichiometry in yttrium-doped barium zirconate: Phase behavior, microstructure, and proton conductivity. *J. Mater. Chem.* **2010**, *20*, 8158–8166. [[CrossRef](#)]
28. Kim, H.-S.; Bae, H.B.; Jung, W.; Chung, S.-Y. Manipulation of Nanoscale Intergranular Phases for High Proton Conduction and Decomposition Tolerance in BaCeO_3 Polycrystals. *Nano Lett.* **2018**, *18*, 1110–1117. [[CrossRef](#)]
29. Holz, L.I.V.; Graça, V.C.D.; Loureiro, F.J.A.; Fagg, D.P. Analysis of the Electrochemical Transport Properties of Doped Barium Cerate for Proton Conductivity in Low Humidity Conditions: A Review. In *Analytical Chemistry-Advancement, Perspective and Applications*; IntechOpen: London, UK, 2020.
30. Kreuer, K.D. On the development of proton conducting materials for technological applications. *Solid State Ion.* **1997**, *97*, 1–15. [[CrossRef](#)]
31. Sarabut, J.; Charojrochkul, S.; Sornchamni, T.; Laosiripojana, N.; Assabumrungrat, S.; Wetwattana-Hartely, U.; Kim-Lohsoontorn, P. Effect of strontium and zirconium doped barium cerate on the performance of proton ceramic electrolyser cell for syngas production from carbon dioxide and steam. *Int. J. Hydrogen Energy* **2019**, *44*, 20634–20640. [[CrossRef](#)]
32. Dubal, S.U.; Bhosale, C.H.; Jadhav, L.D. Performance of spray deposited Gd-doped barium cerate thin films for proton conducting SOFCs. *Ceram. Int.* **2015**, *41*, 5607–5613. [[CrossRef](#)]
33. Chopdekar, R.V.; Arenholz, E.; Suzuki, Y. Orientation and thickness dependence of magnetization at the interfaces of highly spin-polarized manganite thin films. *Phys. Rev. B* **2009**, *79*, 104417. [[CrossRef](#)]
34. Sato, T.; Inoue, T.; Ichinose, D.; Funakubo, H.; Uchiyama, K. Fabrication of highly (110)-oriented BaCeO . *Jpn. J. Appl. Phys.* **2016**, *55*, 02BC19. [[CrossRef](#)]
35. Campos Covarrubias, M.S.; Sriubas, M.; Bockute, K.; Winiarz, P.; Miruszewski, T.; Skubida, W.; Jaworski, D.; Bartmański, M.; Szkodo, M.; Gazda, M.; et al. Properties of Barium Cerate Thin Films Formed Using E-Beam Deposition. *Crystals* **2020**, *10*, 1152. [[CrossRef](#)]
36. Bischof, C.; Nenning, A.; Malleier, A.; Martetschlager, L.; Gladbach, A.; Schafbauer, W.; Opitz, A.; Bram, M. Microstructure optimization of nickel/gadolinium-doped ceria anodes as key to significantly increasing power density of metal-supported solid oxide fuel cells. *Int. J. Hydrogen Energy* **2019**, *44*, 31475–31487. [[CrossRef](#)]
37. Aryanto, D.; Marwoto, P.; Sudiro, T.; Wismogroho, A.S. Sugianto Growth of *a*-axis-oriented Al-doped ZnO thin film on glass substrate using unbalanced DC magnetron sputtering. *J. Phys. Conf. Ser.* **2019**, *1191*, 012031. [[CrossRef](#)]
38. Kimura, T.; Miura, Y.; Fuse, K. Texture Development in Barium Titanate and PMN-PT Using Hexabarium 17-Titanate Heterotemplates. *Int. J. Appl. Ceram. Technol.* **2005**, *2*, 15–23. [[CrossRef](#)]
39. Kimura, T.; Yi, Y.; Sakurai, F. Mechanisms of Texture Development in Lead-Free Piezoelectric Ceramics with Perovskite Structure Made by the Templated Grain Growth Process. *Materials* **2010**, *3*, 4965–4978. [[CrossRef](#)] [[PubMed](#)]
40. Bae, K.; Jang, D.Y.; Jung, H.J.; Kim, J.W.; Son, J.-W.; Shim, J.H. Micro ceramic fuel cells with multilayered yttrium-doped barium cerate and zirconate thin film electrolytes. *J. Power Sources* **2014**, *248*, 1163–1169. [[CrossRef](#)]
41. Andersson, A.K.E.; Selbach, S.M.; Knee, C.S.; Grande, T. Chemical Expansion Due to Hydration of Proton-Conducting Perovskite Oxide Ceramics. *J. Am. Ceram. Soc.* **2014**, *97*, 2654–2661. [[CrossRef](#)]
42. Shukla, S.; Seal, S.; Vij, R.; Bandyopadhyay, S. Reduced Activation Energy for Grain Growth in Nanocrystalline Ytria-Stabilized Zirconia. *Nano Lett.* **2003**, *3*, 397–401. [[CrossRef](#)]
43. Laukaitis, G.; Jauneika, M.; Dudonis, J.; Katkauskas, O.; Milcius, D. The properties of samarium doped ceria oxide thin films grown by e-beam deposition technique. *Vacuum* **2009**, *83*, S114–S117. [[CrossRef](#)]
44. Virbukas, D.; Laukaitis, G.; Dudonis, J.; Milcius, D. The properties of scandium and cerium stabilized zirconium thin films formed by e-beam technique. *Solid State Ion.* **2011**, *188*, 46–49. [[CrossRef](#)]

45. Pergolesi, D.; Fabbri, E.; D'Epifanio, A.; Di Bartolomeo, E.; Tebano, A.; Sanna, S.; Licoccia, S.; Balestrino, G.; Traversa, E. High Proton Conduction in Grain-Boundary-Free Yttrium-Doped Barium Zirconate Films Grown by Pulsed Laser Deposition. *Nat. Mater.* **2010**, *9*, 846–852. [[CrossRef](#)]
46. Aziz, M.J. Film growth mechanisms in pulsed laser deposition. *Appl. Phys. A* **2008**, *93*, 579–587. [[CrossRef](#)]
47. Stefan, E.; Stange, M.; Denonville, C.; Larring, Y.; Hildenbrand, N.; Norby, T.; Haugrud, R. Layered Microstructures Based on BaZr_{0.85}Y_{0.15}O_{3-δ} by Pulsed Laser Deposition for Metal-Supported Proton Ceramic Electrolyser Cells. *J. Mater. Sci.* **2017**, *52*, 6486–6497. [[CrossRef](#)]
48. Saha, B.; Chaturvedi, P.; Yadav, A.K.; Saha, D.; Ganguly, S. Pulsed laser deposition of highly oriented stoichiometric thin films of topological insulator Sb₂Te₃. *J. Vac. Sci. Technol. B* **2016**, *34*, 021806. [[CrossRef](#)]
49. Shin, B.; Leonard, J.P.; McCamy, J.W.; Aziz, M.J. Comparison of morphology evolution of Ge(001) homoepitaxial films grown by pulsed laser deposition and molecular-beam epitaxy. *Appl. Phys. Lett.* **2005**, *87*, 181916. [[CrossRef](#)]
50. Shin, B.; Aziz, M.J. Kinetic-energy induced smoothening and delay of epitaxial breakdown in pulsed-laser deposition. *Phys. Rev. B* **2007**, *76*, 085431. [[CrossRef](#)]
51. Shim, J.H.; Park, J.S.; An, J.; Gür, T.M.; Kang, S.; Prinz, F.B. Intermediate-Temperature Ceramic Fuel Cells with Thin Film Yttrium-Doped Barium Zirconate Electrolytes. *Chem. Mater.* **2009**, *21*, 3290–3296. [[CrossRef](#)]
52. Orava, J.; Kohoutek, T.; Wagner, T. Deposition techniques for chalcogenide thin films. In *Chalcogenide Glasses*; Woodhead Publishing: Sawston, UK, 2014; pp. 265–309. ISBN 978-0-85709-345-5.
53. Gilardi, E.; Fabbri, E.; Bi, L.; Rupp, J.L.M.; Lippert, T.; Pergolesi, D.; Traversa, E. Effect of Dopant–Host Ionic Radii Mismatch on Acceptor-Doped Barium Zirconate Microstructure and Proton Conductivity. *J. Phys. Chem. C* **2017**, *121*, 9739–9747. [[CrossRef](#)]
54. Magrasó, A.; Ballesteros, B.; Rodríguez-Lamas, R.; Sunding, M.F.; Santiso, J. Optimisation of growth parameters to obtain epitaxial Y-doped BaZrO₃ proton conducting thin films. *Solid State Ion.* **2018**, *314*, 9–16. [[CrossRef](#)]
55. Fluri, A.; Marcolongo, A.; Roddatis, V.; Wokaun, A.; Pergolesi, D.; Marzari, N.; Lippert, T. Enhanced Proton Conductivity in Y-Doped BaZrO₃ via Strain Engineering. *Adv. Sci.* **2017**, *4*, 1700467. [[CrossRef](#)]